

Many facets of interferometry: a deceptively simple and powerful measurement technique

Marija Strojnik
Centro de Investigaciones en Óptica
Apdo. Postal 1-948, C.P. 37000, León, México
e-mail: mstrojnik@gmail.com

Abstract

Interferometry is a deceptively simple and yet powerful optical concept, just as Dean Wyant is an unpretentious man who achieved successes by wisely practicing his art. We take two coherent waves and generate an interferometric pattern that gives us an intensity distribution with varying spatial frequencies. We apply several modalities in our laboratory in the CIO: vectorial shearing interferometry to probe a surface in an arbitrary direction, rotational shearing interferometry to detect a faint off-axis source in the presence of a strong, rotationally symmetric one, and interferometry with ballistic photons to diagnose abnormal tissue.

Keywords: interferometry, rotational shearing interferometer, vectorial shearing interferometer, wavefront derivative, aberrations, ballistic photons, transillumination, tissue, testing, instrumentation

1. Introduction

We have been using interferometry in several experiments and engineering solutions. Potentially the most interesting one is the proposal of using the rotationally shearing interferometry to directly detect an extrasolar planet [1-8]. Furthermore, we investigated the use of vectorial shearing interferometers to measure *asphericity* of a sphere, used as a volume standard [9-14]. Along the way, we developed a novel technique to interpret interferograms and apply it to the shape determination [15-22].

Transillumination of *in vivo* samples has been used in medicine to determine the health status of internal organs, teeth, and blood. For the first two, x-rays and positrons might be used in transillumination. Their images could be described as shadows of the object, not including the phase information. Visible and near IR radiation is implemented routinely, for example in oximetry, to assure that the patient has sufficiently oxygenated [23,24]. Interestingly, the amount of transmitted radiation is not important for as long as we obtain measurable signal. In oximetry, two sources of radiation are needed to provide signal to determine the state of oxygenation.

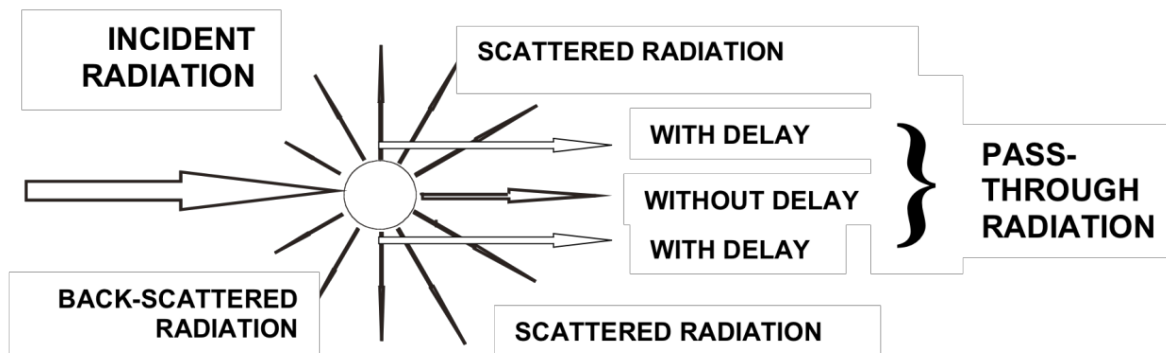


Fig. 1. When the incident radiation impinges on an occlusion, the radiation traveling in forward direction includes the ballistic photons, suffering no phase or direction change, and scattered radiation that undergoes such change.

We wanted to measure the amount of transmitted visible / near IR radiation. It has the advantages that it is not damaging to the tissues. This radiation would be transmitted through tissue without scattering or deflection, as illustrated in Fig. 1. It would maintain its state of coherence, not counting the path delays. When the incident radiation impinges on an occlusion, the radiation traveling in forward direction includes the ballistic photons, suffering no phase or direction change, and scattered radiation that suffers phase and direction change. Thus, this ballistic beam could be used in an interferometric setup to measure the sample transmittance. An additional advantage of the interferometric beam detection is that the scattered radiation that represents most of the transilluminated radiation is ignored, because it lost coherence [25-29].

We were able to obtain good oximetry results for transillumination through the arm of a thin teenager (small amount of fat). The visible / IR radiation is relatively poorly transmitted through the tissue so its application would be limited to thin body parts and small parts of (small) animals. First, we review the transillumination theory with ballistic photons. The experiment was previously used to determine the coefficient of scattering and absorption of laboratory prepared liquids. Then, we present some simulation results.

2. Experimental – interference of ballistic photons

A 3-mW HeNe laser (Oriel), emitting radiation at 633 nm, provides the coherent illumination. In the actual applications of tissue characterization, the near IR wavelengths are preferable due to the advantageous spectral characteristics of biological tissues of decreased scattering and absorption in this spectral region. The visible wavelengths have an obvious advantage during the feasibility assessment and characterization of this technique.

A small-diameter laser beam is used to sample a correspondingly small area on the tissue to achieve high spatial resolution of the probe. In practice, this probe beam may be scanned over the complete sample area to evaluate its spatially dependent transmission characteristics. The beam passes through the microscope objective that spatially filters it and expands it. The square box at the output of the laser represents schematically the objective and the diaphragm. An aperture delineating the spatial extend of the probe beam defines the spatial resolution on the object, making it smaller than the actual diameter of the laser beam.

Inside the sample, the radiation may be singly or multiply scattered, depending on the number of scattering particles per beam volume. The rays may scatter into a full sphere. However, for the transmission and subsequent detection of the ballistic photons, the forward scattered radiation represents a highly detrimental noise that must be eliminated. Any ray, that suffers ever so small deviation from either its original direction or its trajectory of propagation, is presumed to have participated in the scattering. Therefore, it represents unwanted noise. The photons that are scattered into a small cone close to the line of forward propagation are eliminated to a high degree with an aperture just after the sample. The aperture transmits only the pass-through ballistic photons.

A beam direction-changing mirror is mounted on a PZT actuator to control the optical path in the sample arm. When the optical path is changed by up to half a wavelength, the phase delay is changed by up to π radians. This allows the signal on the detector to oscillate between zero when reference and ballistic beam are out of phase to maximum modulation when they are in phase. Beam splitters are used to divide and then to recombine the beams. The first one, just a polished plane parallel piece of glass, transmits most of the power into the arm with the sample, at 98/2 power ratio. In the sample arm, most of the radiation is expected to be lost upon scattering and/or absorption in trans-illuminated samples, such as biological tissues.

In the reference arm with 2% transmitted power there are only two optical components: a beam direction-changing mirror and a variable-transmission (gray) filter that may be adjusted for maximum contrast of the interferometric pattern, as judged by a human observer, depending on the maximum sample density. Then, both beams have approximately the same power onto the detector plane, resulting in the maximum visibility. This component provides potential for the wave attenuation by a factor of 10^{-3} . This corresponds to the power attenuation of 10^{-6} .

The signal transmitted through the sample is encoded as the amplitude of the eye-pattern with a phase-modulation scheme. Employing the piezoelectric actuator (PZT) for controlled mirror displacement in the sample arm, the optical path travelled by the ballistic photons may be modified to compensate the phase delay introduced by the sample and optical components. The detected power is triggered to record the highest value (amplitude) of the interference signal. This value corresponds to the product of waves in the reference and the sample arm at the detector when the waves are in phase.

The reference beam and the sample beam overlap at the second beam splitter and volume behind it. As the beam splitter is partially reflective and partially transmissive, the interference pattern is created above it and to its right. In the diagram of Fig. 2, we transposed the pass-through and the reflected beams at the second beam splitter so that this figure may occupy less space. The pass-through, highly attenuated beam of ballistic photons is transmitted again at the second beam splitter, with the transmission ratio of 98/2, expanding the dynamic range by a factor of one hundred once again.

The ballistic photons pass through the third pinhole, with diameter equal to that of the second one. The function of the second contrast enhancement aperture (the third pinhole) is to clip any slightly divergent or scattered rays that might have remained in the beam. Just after the pinhole, a lens is used to project the overlapping radiation from both arms of the interferometer onto the detector surface. A low-light-level, highly sensitive Apogee camera featuring 4000 by 4000 pixels detects this weak radiation.

Two beam splitters at 10^2 each and gray level neutral density filter at 10^3 bring the wave dynamic range of this experimental arrangement to 10^7 , all achievable with the off-the-shelf optical components. This means that 1 transmitted photon among 10^{14} incident ones may be measured to provide useful results. This corresponds to the expected power attenuation in the tissue of 10^{-14} . Thus, this technique may be used on a tissue that appears quite opaque upon examination with unaided eyes to provide information about its volume in-homogeneities.

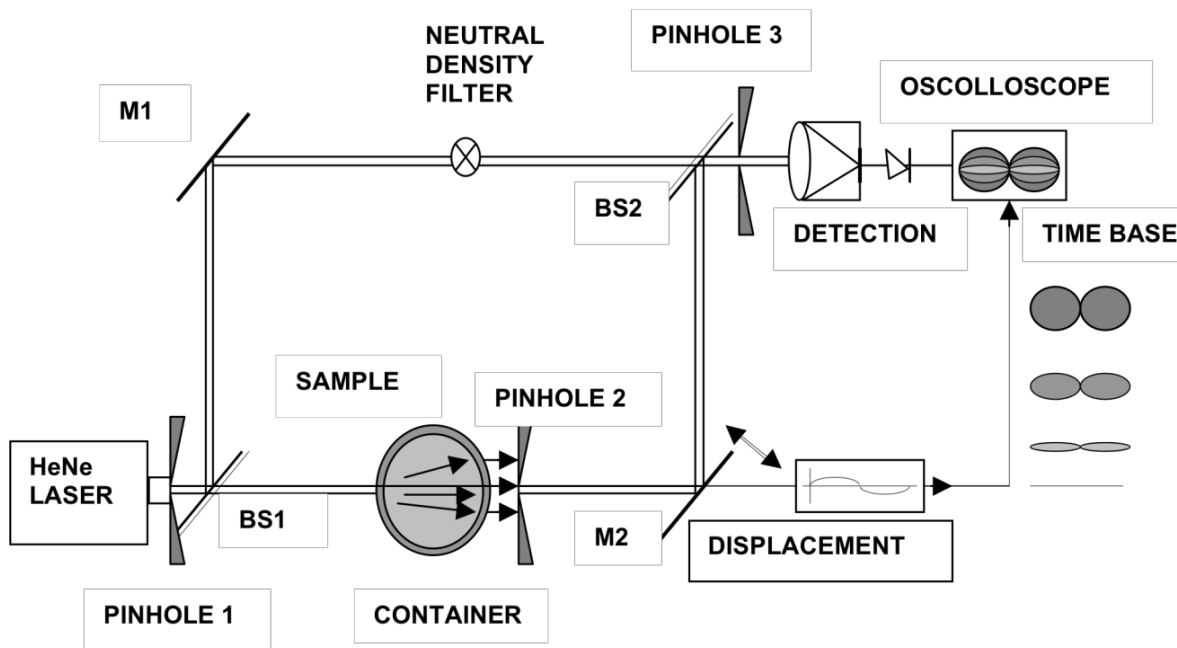


Fig. 2. In a transillumination experiment, ballistic photons are separated from the scattered ones by combining them in a Mach Zehnder interferometer. The sample is examined at a single point and scanned to obtain transmission function in transverse plane.

3. Theory

The power P at point (x,y) upon interference between ballistic beam transmitted through the sample and the one traveling through the reference arm was found previously [31]. Subscript sa (ra) denotes sample (reference) arm. [W]

$$P(x,y;t) = \tau_g^2 P_{sa} \exp\left\{-\sum_i D_i(x,y)(k_{sci} + \alpha_i)\right\} + P_{ra} + 2 \tau_g [P_{sa} P_{ra}]^{1/2} \exp\left[-\left(\frac{1}{2}\right)\sum_i D_i(x,y)(k_{sci} + \alpha_i)\right] \cos\left\{\varphi_0 + \left(\frac{2\pi}{\lambda}\right)\sum_i [D_i(x,y) n_{si} - ct n_a]\right\} \quad (1)$$

In this equation, τ_g is the transmission loss of the container, P_{sa} is the power into the sample arm, P_{ra} is the power into the reference arm, D_i is a distance that a ballistic photon travels through material i , k_{sci} and α_i are the scattering and absorption coefficients of the sample segment, φ_0 is a delay, and $D_i n_{si}$ is the optical path through the sample segment i . The first term in this equation is a constant for a specific sample and experimental conditions. It may be eliminated using a low-pass filter. We introduced time dependence in the second term by including a movable mirror attached to a piezoelectric actuator. We graph the second term as a function of time in Fig. 2. The maximum transmitted power is found upon letting cosine be equal to one.

$$P_{\max}(x,y;t) = \left\{P_{ra}^{1/2} + \tau_g P_{sa}^{1/2} \exp\left[-\left(\frac{1}{2}\right)\sum_i D_i(x,y)(k_{sci} + \alpha_i)\right]\right\}^2 \quad (W) (2)$$

The minimum transmitted power is found upon letting cosine be equal to minus one.

$$P_{\min}(x,y) = \left\{P_{ra}^{1/2} - \tau_g P_{sa}^{1/2} \exp\left[-\left(\frac{1}{2}\right)\sum_i D_i(x,y)(k_{sci} + \alpha_i)\right]\right\}^2 \quad (W) (3)$$

The average power is found by taking one half of the sum of Eq. 2 and 3.

$$P_{ave}(x,y) = P_{ra} + \tau_g^2 P_{sa} \exp\left\{-\sum_i D_i(x,y)(k_{sci} + \alpha_i)\right\} \quad (W) (4)$$

The amplitude is found by subtracting the average in Eq. 4 from total power in Eq. 1.

$$P_{amp}(x,y) = 2 \tau_g [P_{sa} P_{ra}]^{1/2} \exp\left[-\left(\frac{1}{2}\right)\sum_i D_i(x,y)(k_{sci} + \alpha_i)\right] \quad (W) (5)$$

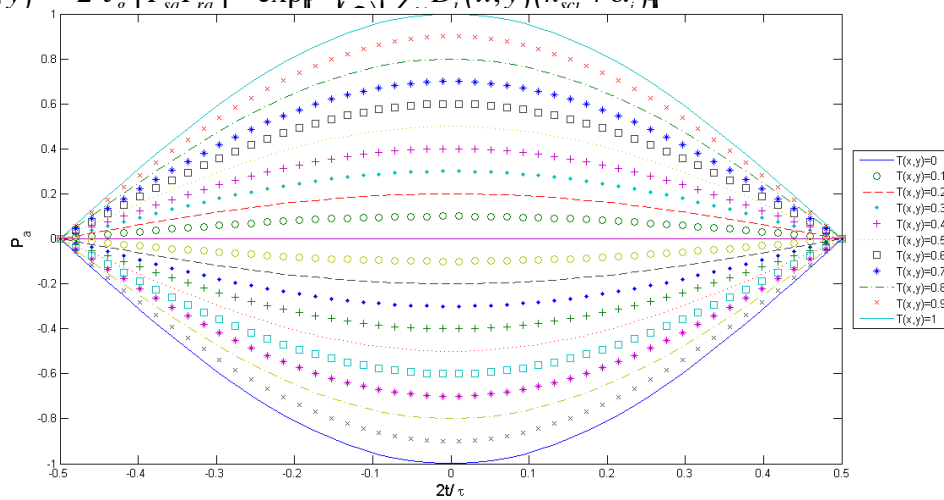


Fig. 3. Power changes as a function of time in the wave cycle, with the medium transmission as a parameter.

We define a parameter V that may be related to the contrast or visibility.

$$V = \frac{2[T(x,y;D_i)P_{sa}P_{ra}]^{1/2}}{T(x,y;D_i)P_{sa}+P_{ra}} \quad (6)$$

We define the signal-to-noise ratio, S/N, in a standard fashion.

$$S/N = [ABS(T_i - T_b) / T_b] \quad (7)$$

Here T_i is the transmission value through the occlusion and tissue and T_b is the background transmission. We selected for T_b the minimum value of the transillumination through the tissue without occlusion. Looking for example at a broken bone, this imagery is sufficient to see the nature and complexity of the fraction.

To detect an unknown abnormality within the bone, the value of S/N must be greater than a reference value V_{ref} . Its choice will likely depend on the experimental arrangement. It will define the detection accuracy of the method. The smaller the reference value that still results in the detection, the greater the accuracy of the method. We introduce the binarization.

$$pixel\ value = \begin{cases} 0, & S/N \leq V_{ref} \\ 1, & S/N > V_{ref} \end{cases} \quad (8)$$

This thresholding allows the assignment of the pixel as belonging to the occlusion or not.

4. Three-tissue transillumination – model with five distances (phalanx)

We model an inclusion inside a bone-like tissue, wrapped inside a flesh-like cylinder, as illustrated in Fig. 4. We consider the inclusion (growth, tumor) to be a sphere in the first approximation, while the outside of body part is a cylinder. The bone is modeled as a cylinder that ends in a sphere, using a hyperbola to model the transition. On the left side of Fig. 4, we show the geometrical model, while on the right side we present the transilluminated signal obtained in the interferometric arrangement. The assumed coefficients of absorption are 0.058 mm^{-1} for bone, 0 mm^{-1} for the occlusion, and 0.07 mm^{-1} for flesh tissue.

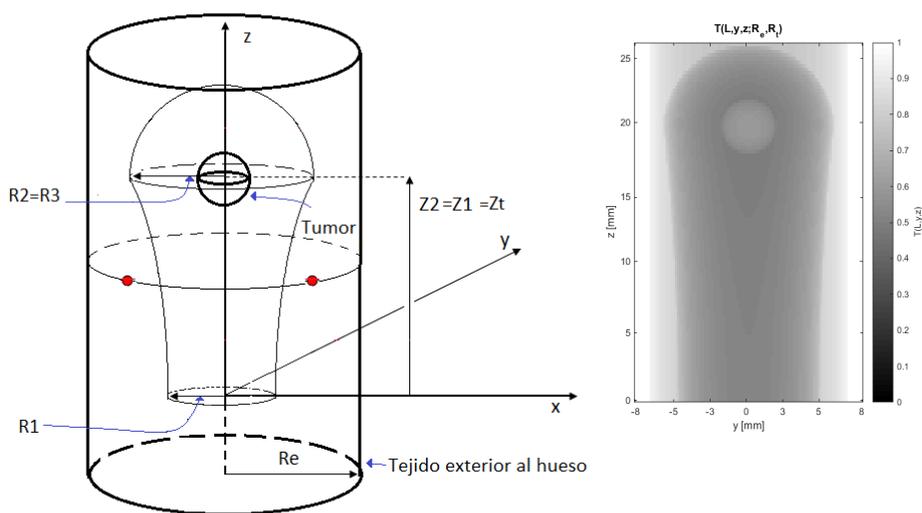


Fig. 4. Left: mathematical model of a three-tissue transillumination problem; right: transmitted signal on the y - z plane.

4.1 Case 1: Transillumination through a healthy tissue (no inclusion)

Figure 5 illustrates the model of healthy phalanx and the transilluminated image, constructed by pointwise transillumination. We consider that the figure is symmetrical with respect to the xz plane. In addition, the objects we model have azimuthal symmetry. This way we consider only the upper half of the representation of the bone. Photons travel along x -axis into the tissue. The darker areas represent places where the optical path through the bone is longer.

We can see that the amount of transmitted radiation decreases for the central part in the sphere. It slowly decreases as the neck of the bone decreases toward axis of symmetry. It also decreases toward the edges of the bone. Considering that the bone is homogeneous, the amount of radiation passing through the sample depends on the distance the light travels and the scattering coefficient.

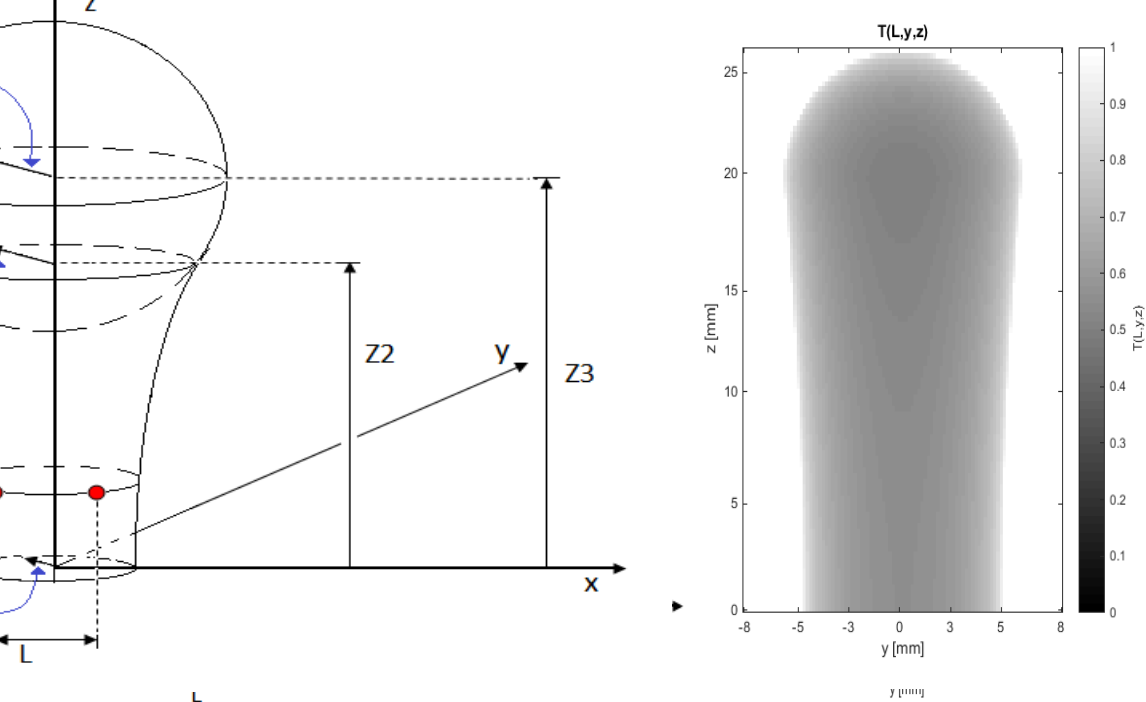


Fig. 5. Left: mathematical model of a representative healthy bone, formed by a sphere and hyperboloidal segments. Right: the trans-illumination signal when the uniform radiation is incident along x -axis.

4.2 Case 2: Trans-illumination through a simulated bone with a round occlusion inside the top sphere

A sphere inside the spherical part of the bone may represent an occlusion, as seen in Fig. 6. The amount of the trans-illuminated radiation is shown on the right. Taking the difference between the data presented in the right sides of Fig. 6 and Fig. 5 yields the image of the occlusion, shown in Fig. 7.

Using Eq. 8, we indicate the values of the pixels in a three-tissue transillumination simulation for different reference values in Table 1. These binarized pixels denote the size of the occlusion. The larger the threshold value, the smaller the detected occlusion appears.

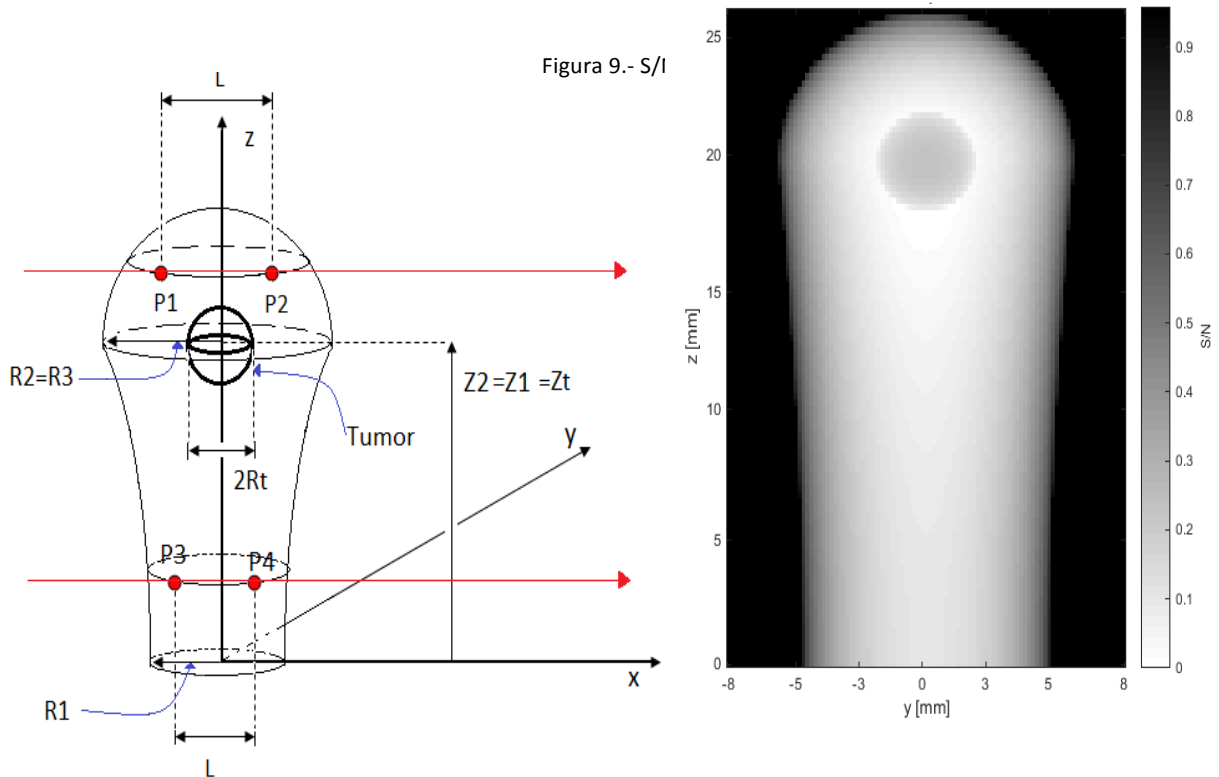


Fig. 6. Left: mathematical model of the bone, with an inclusion of radius R_t at the center of the top sphere. Right: the trans-illuminated radiation exiting the bone in the y-z plane.

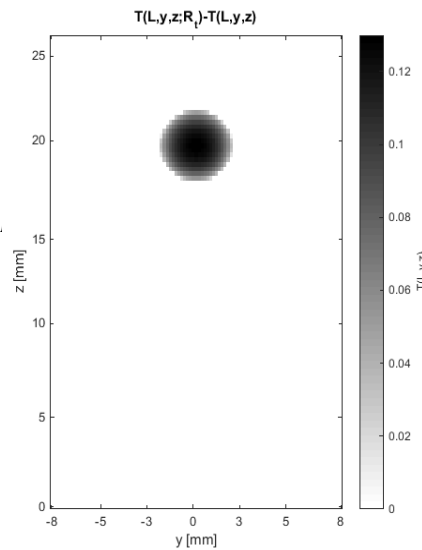


Fig. 7. Difference in the transillumination through the bone with and without an occlusion.

Table 1. The size of detected tumor vs threshold value for the same occlusion size.

Ref. value	Bone and occlusion	Flesh, bone, and occlusion
$V_{ref} \geq 0.1$		
$V_{ref} \geq 0.15$		
$V_{ref} \geq 0.2$		
$V_{ref} \geq 0.25$		

5. Summary

We demonstrated that some visible /near infrared radiation is transmitted even through relatively thick biological in-vivo samples, such as finger and arm. We proposed that those ballistic photons can be used in an interferometric arrangement to add them constructively in a heterodyne detection setup. We used a calibrated setup to determine separately the absorption coefficient and the scattering coefficient of samples, giving us confidence that this technique can be used for diagnosis of thinner body parts, especially for small animals.

Acknowledgments. Some of this material is based upon work supported by the Air Force Office of Scientific Research, under contract AFOSR (FA9550-18-1-0454). Any opinions, finding, and conclusions or recommendations expressed in this presentation are author's and do not necessarily reflect the views of the United States Air Force. Ms. B. Guzman is thanked for technical assistance.

6. References

1. M. S. Scholl, "Signal detection by an extra-solar-system planet detected by a rotating rotationally-shearing interferometer," *J. Opt. Soc. Am. A*, **13** (7), 1584- 1592 (1996). <http://doi.org/10.1364/JOSAA.13.001584>
2. M. Strojnik, "Simulated interferometric patterns generated by a nearby star-planet system and detected by a rotationally-shearing interferometer," *J. Opt. Soc. Am. A*, **16** (8), 2019-2024 (1999). <https://doi.org/10.1364/JOSAA.16.002019>
3. 87. C. Vasquez-Jaccaud, M. Strojnik, G. Paez, "Effects of a star as an extended body in extra-solar planet search," *J. Mod. Optics* **57** (18, 20), pp 1808–1814 (2010). <https://doi.org/10.1080/09500340.2010.528564>
4. M. Strojnik, "Extrasolar planet observatory on the far side of the Moon," *J. Appl. Remote Sens.*, **8** (1), 084982 (2014). <https://doi.org/10.1117/1.JRS.8.084982>
5. M. S. Strojnik, M. S. Kirk, "Telescopes," in *Fundamentals and basic optical instruments*, D. Malacara, B. Thompson, Eds., 325-375; ISBN: 9781498720748 (hardback), ISBN 9781315119984 (e-book) 207-26, CRC Press, New York, New York (2018).
6. M. Strojnik, B. Bravo-Medina, "Rotationally shearing interferometer for extra-solar planet detection: preliminary results with a solar system simulator," *Optics Express*, Vol. 28(20), 28 September 2020. <https://doi.org/10.1364/OE.398649>
7. R. Gonzalez-Romero, M. Strojnik, and G. Garcia-Torales, "Theory of a rotationally shearing interferometer," Vol. 38 (2) / February 2021 / 264-270, *JOSA-A*. <https://doi.org/10.1364/JOSAA.406186>
8. B. Bravo-Medina, M. Strojnik, A. Mora-Nuñez, H Santiago- Hernández, "Rotational-shearing-interferometer response for a star-planet system without star cancellation," *Appl. Sci.* **2021**, *11*, 3322. <https://doi.org/10.3390/app11083322>
9. G. García-Torales, M. Strojnik, "Simulations and experimental results with a vectorial shearing interferometer," *Opt. Eng.*, **40** (5), 767-773 (2001). <https://doi.org/10.1117/1.1360707>
10. G. García-Torales, M. Strojnik, "Risley prisms to control wave-front tilt and displacement in a vectorial shearing interferometer," *Appl. Opt.*, **41** (7) 1380-1384 (2002). <https://doi.org/10.1364/AO.41.001380>
11. M. Strojnik, M. Mantravadi, "Lateral Shearing Interferometry," in *Optical Shop Testing*, ISBN: 978-0-471-48404-2 D. Malacara, Eds., pp 122-176, John Wiley & Sons, Inc (2007).
12. G- Garcia-Torales, G. Páez, M. Strojnik, J. Villa, J. L. Flores, A. Gonzalez Alvarez, "Experimental intensity patterns-obtained from a 2D shearing interferometer with adaptable sensitivity," *Opt. Comm.* **257**, 16-26 (2006). <http://doi.org/10.1016/j.optcom.2005.07.014>
13. C. N. Ramirez, M. Strojnik, "Performance evaluation for a wave-front displacement system for vectorial shearing interferometer," *Opt. Com.*, **281**, 347 -355 (2008). <http://dx.doi.org/10.1016/j.optcom.2007.07.043>
14. C. Ramirez, M. Strojnik, "Estimation of the degree asphericity of a glass sphere using a vectorial shearing interferometer," *Opt. Commun.* **284** (2011), 1517-1525. <https://doi.org/10.1016/j.optcom.2010.10.017>
15. G. Paez, M. Strojnik, "Convergent, recursive phase reconstruction from noisy, modulated intensity patterns using synthetic interferograms," *Opt. Lett.* **23**(6) 406-408 (1998). <https://doi.org/10.1364/OL.23.000406>
16. G. Paez, M. Strojnik, "Fringe analysis and phase reconstruction from modulated intensity patterns," *Opt. Lett.*, **22**(22), 1669-1971 (1997). <https://doi.org/10.1364/OL.22.001669>
17. G. Paez, M. S. Scholl, "Phase-shifted interferometry without phase unwrapping: reconstruction of a decentered wavefront," ISSN:1084-7529 *J. Opt. Soc. Am. A*, **16** 475-480 (1999). <https://doi.org/10.1364/JOSAA.16.000475>

18. J. Muñoz, M. Strojnik, "Phase recovery from a single undersampled interferogram," ISSN: 2155-3165 *Appl. Opt.*, **42** (34), 6846 - 6855 (2003). <http://doi.org/10.1364/AO.42.006846>
19. J. Muñoz, M. Strojnik, "Two-dimensional phase unwrapping of subsampled phase-shifted interferograms," ISSN 0950 -340, *J. of Mod. Opt.* **51** (1), 49-64 (2004). <https://doi.org/10.1080/09500340408234591>
20. J. L. Flores, M. Strojnik, A. Muñoz, G. Garcia-Torales, S. Ordoñez, A. Cruz, "Dynamic 3D shape measurement by iterative phase shifting algorithms and colored fringe patterns," *Opt. Express* **26**, 12403-12414 (2018). <https://doi.org/10.1364/OE.26.012403>.
21. J. L. Flores, M. Strojnik, A. Muñoz, G. Garcia-Torales, S. Ordoñez, A. Cruz, "Dynamic 3D shape measurement by iterative phase shifting algorithms and colored fringe patterns," *Opt. Express* **26**, 12403-12414 (2018). <https://doi.org/10.1364/OE.26.012403>.
22. M. Strojnik, M. Kujawinska, D. Malacara, "Metrology of full-field methods," *Advanced optical instruments and techniques*, D. Malacara, B. Thompson, Eds., 213-244; ISBN: 9781498720670 (hardback), ISBN 9781315119977 (e-book), CRC Press, New York, New York (2018).
23. C. Vasquez-Jacaud, M. Strojnik, "Wavelength selection method with standard deviation: application to pulse oximetry," ISSN: 0090-6964, *Annals of Biomedical Engineering* **39** (7), pp 1994-2009 (2011). <https://doi.org/10.1007/s10439-011-0304-7>
24. F. Corral, M. Strojnik, "A photoplethysmographic imaging system with supplementary capabilities," *Optica Applicata*, **2**, Vol. **44** (2014). ISSN: 1899-7015. <https://doi.org/10.5277/oa140202>
25. P. Vacas-Jaques, M. Strojnik, "Pass-through photon-based biomedical transillumination," ISSN: 1083-3668 *J. Biomed. Opt.* **13**, 0413071-10 (2008). <https://doi.org/10.1117/1.2953191>
26. P. Vacas-Jacques, M. Strojnik, "Forward-calculated analytical interferograms in pass-through photon-based biomedical transillumination," *JOSA A* **26**, (3), 602-612 (2009). <https://doi.org/10.1364/JOSAA.26.000602>
27. P. Vacas-Jacques, V. Ryabukho, M. Strojnik, V. Tuchin, "Theoretical diffractive filter performance for ballistic transillumination," *Компьютерная оптика* ISSN: 0955-3 (*Computer Optics*), **36** (2) 129-137 (2009).
28. P. Vacas-Jacques, M. Strojnik, "Effects of spectral dependence in pass-through photon-based biomedical transillumination," ISSN: 1793-7205 *Journal of Innovative Optical Health* **2**, 235-244 (2009). <https://doi.org/10.1142/S179354580900053X>.
29. P. Vacas-Jacques, V. Ryabukho, M. Strojnik, V. Tuchin, "Ballistic auto-correlation interferometry," ISSN 2076-2518, *Journal of Saratov State University* (2009).
30. F. Corral, M. Strojnik, "Tissue characterization with ballistic photons: counting scattering and/or absorption centres," *Opto-Electronics Review* **23**(1), 44-52 (2015). <https://doi.org/10.1515/oere-2015-0011>
31. M. Strojnik, "Interferometric Tissue Characterization: I. Theory," *Infrared Spaceborne Remote Sensing XIII*, San Diego, CA, USA, Proc. SPIE 5883, 58830Y1-12 (2005). <https://doi.org/10.1117/12.621274>